NASA TECHNICAL MEMORANDUM
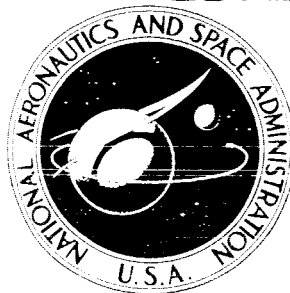
NASA TM X-1137

UB
NASA TM X-1137

COMPARISON OF FREE-FLIGHT AND CONVENTIONAL WIND-TUNNEL STABILITY TESTS FOR APOLLO COMMAND MODULE AND ABORT CONFIGURATIONS

by Gerald N. Malcolm and Donn B. Kirk

Ames Research Center

Moffett Field, Calif.

COMPARISON OF FREE-FLIGHT AND CONVENTIONAL WIND-TUNNEL

STABILITY TESTS FOR APOLLO COMMAND MODULE

AND ABORT CONFIGURATIONS

By Gerald N. Malcolm and Donn B. Kirk

Ames Research Center
Moffett Field, Calif.

NATIONAL AERONAUTICS AND SPACE ADMINISTRATION

COMPARISON OF FREE-FLIGHT AND CONVENTIONAL WIND-TUNNEL

STABILITY TESTS FOR APOLLO COMMAND MODULE

AND ABORT CONFIGURATIONS*

By Gerald N. Malcolm and Donn B. Kirk
Ames Research Center

SUMMARY

19131

Free-flight tests were conducted at subsonic and low supersonic speeds to determine the static and dynamic stability characteristics of three Apollo abort configurations: command module alone, command module with aerodynamic strakes, and command module plus escape tower with flap. All of the models were launched in the apex-forward attitude and large-amplitude, nearly planar motions were observed. Since a new technique was required for analyzing large-amplitude data, the question was examined whether computer-synthesized motions, based on conventional wind-tunnel experimental results, could be made to match the observed motions. In general, it was possible to get good agreement between the observed and synthesized motions. The command module alone was statically and dynamically stable in the apex-forward attitude. The other two configurations performed their expected turn-around maneuver to a heat-shield-forward attitude but did not immediately maintain this attitude and in some cases did not maintain it at all. Conf.

INTRODUCTION

A necessary and important part of Project Apollo, a manned lunar-exploration project, is the launch escape system to be employed when an abort prior to atmospheric exit is necessary. The abort maneuver consists of separating the command module from the booster by means of an escape rocket and, after a short period of power-off free flight following escape-rocket burnout, properly reorienting the command module for descent with the heat shield forward. The heat shield must be forward for proper deployment of the parachute.

Conventional wind-tunnel data (unpublished) indicated that at subsonic and low supersonic speeds the command module alone was stable in the apex forward attitude and would not reorient itself to a heat-shield-forward attitude. The NASA Manned Spacecraft Center requested that free-flight tests be made to confirm this result and to determine whether two proposed configurations would eliminate this apex-forward trim point. One of these configurations was simply the command module with strakes added in the transverse plane of geometric symmetry; the other consisted of the command module plus the launch escape tower with a flap. The purpose of these additions to the basic
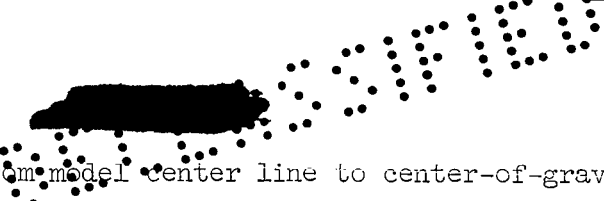
Unclassified.

command module was to produce a positive pitching moment that would eliminate any stability in the apex-forward attitude. All the configurations were tested in the Ames Pressurized Ballistic Range and all were launched in an apex-forward attitude.

The large-amplitude motions of the models in free-flight tests, and the inherent nonlinearities in the aerodynamic coefficients, made it impractical to obtain these coefficients in a straightforward manner. Instead, the reverse problem was considered, that of determining whether synthesized motions based on conventional wind-tunnel data could be made to match the nearly planar free-flight motions.

SYMBOLS

A — frontal area

C_L — lift coefficient, $\dfrac{\text{lift}}{qA}$

C_{L_σ} — local rate of change of C_L with σ, $\dfrac{\partial C_L}{\partial \sigma}$, per rad

C_m — pitching-moment coefficient, $\dfrac{\text{pitching moment}}{qAd}$

$(C_{m_q} + C_{m_{\dot\sigma}})$ — damping-in-pitch derivative, $\dfrac{\partial C_m}{\partial\left(\dfrac{\dot\theta d}{V}\right)} + \dfrac{\partial C_m}{\partial\left(\dfrac{\dot\sigma d}{V}\right)}$, per rad

d — maximum diameter of model

I_y — moment of inertia about a transverse axis through the center of gravity and perpendicular to the plane of mass symmetry

m — mass of model

q — free-stream dynamic pressure

R — Reynolds number based on maximum diameter and free-stream conditions

r_g — radius of gyration, $\sqrt{I_y/m}$

t — independent variable (time) for synthesized motion plots

V — velocity along flight path

X_{cg} — axial distance from center of heat shield to center-of-gravity position

Z_{cg} transverse distance from model center line to center-of-gravity position

α angle of attack (in the vertical plane) ($\alpha = 0$ corresponds to apex-forward attitude)

β angle of sideslip (in the horizontal plane) ($\beta = 0$ corresponds to apex-forward attitude)

γ angle between flight path and horizontal

θ angle between body axis and horizontal

ρ free-stream air density

σ resultant angle of attack, $\tan^{-1}\sqrt{\tan^2\alpha + \tan^2\beta}$

MODELS AND TEST CONDITIONS

Details of the command module and the two turn-around models are sketched in figure 1. The command module was machined from 7075-T6 aluminum and the center of gravity was offset by a cylinder of tungsten alloy inserted through the model off the model center line. The strakes (fig. 1(a)) were made of aluminum and glued into slots in the command module. The tower (fig. 1(b)) was constructed from steel drill rod and assembled with a high-strength solder. The tower members are about 75 percent larger in diameter than the true scaled size so as to withstand the gun launching. The flap attached to the tower structure was made of brass sheet. Photographs of the models are given in figure 2.

The models were gun launched into the Ames Pressurized Ballistic Range, where time-distance histories and attitude histories were recorded at 24 spark shadowgraph stations along its 203-foot length. The models were launched in an apex-forward attitude into still air at atmospheric pressure over a Mach number range from 0.33 to 2.05. Reynolds numbers varied from 0.40×10^6 to 2.3×10^6 based on free-stream conditions and model diameter. One model of the command module alone was launched into still air at 2.8 atmospheres to observe flow details on the model and detect differences, if any, in stability resulting from a full-scale Reynolds number. For this test the average Reynolds number was 3.43×10^6.

The physical characteristics of the models and the respective flight conditions for each test are summarized in table I.

DATA REDUCTION

The purpose of the tests on both the command module alone and the turn-around configurations was to observe the motion of these bodies in free flight

starting with an initial attitude of apex forward (heat shield aft), and to determine, if possible, meaningful aerodynamic coefficients. As expected, the resulting angular motions were either of very high amplitude or tumbling. In all cases, the motion was nearly planar and roll rates were small enough to be considered negligible.

Free-flight oscillatory motions of low amplitude can usually be reduced and analyzed so that aerodynamic stability coefficients can be extracted directly from the frequency and amplitude history of the motion. However, for bodies with nonlinear pitching moments that oscillate through large amplitudes, such as encountered in the present tests, the derivation of meaningful stability coefficients in this manner is nearly impossible unless data are recorded continuously. A different approach was therefore necessary for analyzing the results.

This approach consisted of determining whether motions synthesized from conventional wind-tunnel experimental results could be made to correspond to the nearly planar motions of large amplitude observed in the free-flight tests. The method was to match the observed angular motion as nearly as possible by matching the model characteristics and free-flight test conditions (i.e., air density and velocity history), and then to integrate numerically on a digital computer the differential equation of angular motion with coefficients provided from conventional wind-tunnel aerodynamic data. The synthesized motion is restricted to planar motion with three degrees of freedom (one rotational, two translational) and, consequently, can be compared only to those free-flight motions that are planar or nearly so. The following equation of angular motion was used to generate the synthetic motions. (See appendix for the development of this equation.)

$$\ddot{\sigma} - \frac{\rho A V}{2m}\left[\left(C_{m_q} + C_{m_{\dot{\sigma}}}\right)\left(\frac{d}{r_g}\right)^2 - C_{L_\sigma}\right]\dot{\sigma} - \frac{C_m \rho V^2 A d}{2 I_y} = 0 \qquad (1)$$

where

$$V = V(t)$$

$$C_m = C_{m_1}(M,\sigma) \quad \text{or} \quad C_{m_2}(V,\sigma)$$

$$C_{L_\sigma} = C_{L_{\sigma_1}}(M,\sigma) \quad \text{or} \quad C_{L_{\sigma_2}}(V,\sigma)$$

Equation (1) was integrated numerically with the coefficients provided as follows:

The constants A, d, I_y, r_g, and m are the model geometric characteristics.

The parameter ρ is free-stream air density of the test and is constant.

The parameter V is the velocity of the model and decreases with time as a result of aerodynamic drag. This parameter was entered into the integration program in the form of a table of V versus t, obtained from the experimental

time-distance histories, and an interpolation technique was used at each step of the integration to determine a value for V. An example of a velocity history is shown in figure 3.

The aerodynamic coefficients were obtained from previously unpublished conventional wind-tunnel experimental results from Ames Research Center, North American Aviation, and Arnold Engineering Development Center. These results are shown in figure 4. The figures show C_m and C_L versus α (α for wind-tunnel data is equivalent to σ for present tests) for each configuration for the appropriate Mach numbers encountered in the free-flight tests.

The parameter C_m is the pitching-moment coefficient and its value varies with both Mach number (or velocity) and angle of attack. A table containing C_m versus σ for each of several different Mach numbers spanning the Mach number range of the test was entered into the program. At each step of the integration, the velocity was determined, as mentioned previously. The angle of attack was determined as a direct result of the integration. From these two pieces of information, the proper value for C_m was obtained by double interpolation in the table.

The parameter C_{L_σ} is the local lift-curve slope at each angle of attack and was calculated from a table of C_L versus σ which was entered into the program for various Mach numbers, as with C_m versus σ. The values of C_{L_σ} at each step of the integration were determined by combining double interpolation in the table with a finite-difference technique to obtain a slope.

The quantity $(C_{m_q} + C_{m_{\dot{\sigma}}})$ is the only undetermined parameter in equation (1). Arbitrary constant values of this parameter (aerodynamic damping) were fed into the program until, by trial and error, the best possible match to the observed motion was obtained. In all cases the motion generated was quite sensitive to the value of $(C_{m_q} + C_{m_{\dot{\sigma}}})$ that was chosen. When data for aerodynamic damping were available (available only for tower-flap models and is shown in figure 5 for M = 0.5 and M = 0.8), they were entered into the program in the form of $(C_{m_q} + C_{m_{\dot{\sigma}}})$ versus σ similar to the C_m versus σ data but only for one Mach number which corresponded closely to the average Mach number of the flight. Interpolation between Mach numbers was not used in this instance. With the aerodynamic damping also specified, all the coefficients of equation (1) were determined and the motion produced was unique.

The initial conditions for starting the integration were matched at the first peak amplitude of the observed motion where $\sigma = \sigma_{peak}$ and $\dot{\sigma} = 0$. The synthesized motions are plotted with t = 0 corresponding to the time when the model emerged from the gun muzzle. The part of the synthesized curve from t = 0 to t_i, the time at which the initial conditions were chosen to start the integration, was obtained by integrating in the direction of decreasing time from t_i to t = 0.

The observed and synthesized motions of each of the three configurations are compared and discussed. All the models exhibited nearly planar motion in flight; therefore, the comparison of observed motions to motions synthesized from equations of planar motion is valid.

Command Module Alone

At the beginning of the test program three exploratory flights of the command module alone were conducted in the first seven stations of the range. The first two tests were conducted at atmospheric pressure at $M \cong 1.1$ and $M \cong 0.7$, respectively. The third was conducted at 2.8 atmospheres pressure at $M = 1.1$ and a typical full-scale Reynolds number of 3.4×10^6. As seen from the faired plots in figure 6, all three show static stability about a trim condition near $\sigma = 40^\circ$. The purpose of the high-pressure test was to determine any important effects of Reynolds number on stability. A comparison of the motion histories of figure 6 and observation of the flow conditions from the shadowgraphs led to the conclusion that there was no significant difference due to Reynolds number.

Figure 7 shows the observed and synthesized motions of a 24-station flight of the command module alone launched at an initial Mach number of 2.05 and decelerating to $M = 1.29$. The initial conditions for the synthesized motion were $\sigma_i = 66^\circ$, $\dot{\sigma}_i = 0$ at $t_i = 0.0115$ second. The synthesized motion that was judged to be the best match to the data was the one which came closest to passing through the data points and at the same time maintained the same peak amplitudes as the faired plot. It can be seen that with its apex forward the command module is both statically and dynamically stable in this Mach number range and oscillates about a trim angle of $\sim 36^\circ$. In general, the synthesized and observed motions match extremely well; however, it is apparent that the observed motion has a slightly higher frequency than the synthesized motion. This difference in frequency would indicate that the free-flight model experienced slightly higher pitching moments than the wind-tunnel data indicate. A value of $(C_{m_q} + C_{m_{\dot{\sigma}}}) = -0.15$ was used to obtain the synthetic plot and therefore represents the average aerodynamic damping for this amplitude range.

It should be noted, both for this case and the following ones, that the synthetic angle that appears at $t = 0$ second is the angle that would have existed at that point had the model been in free rotation from $t = 0$ to t_i. This is not the case, however, because there is a finite period of time after emergence from the gun in which the model rotation is affected by sabot separation and flow establishment.

Figure 8 shows the observed data points and the synthesized motions which best matched the observed points for two flights of the command module with strakes. For the first flight (fig. 8(a)) the model was launched at an initial Mach number of $M = 1.10$ and decelerated to $M = 0.73$. The initial conditions for the synthesized motion were $\sigma_i = 200^\circ$, $\dot{\sigma}_i = 0$, at $t_i = 0.026$ second. For the first part of the motion, from $t = 0$ to $t = 0.101$ second, where the model is traversing large angular excursions, $(C_{m_q} + C_{m_{\dot{\sigma}}}) = -0.135$ gave the best match. It was found that when the motion was generated to the completion time of $t = 0.22$ second with $(C_{m_q} + C_{m_{\dot{\sigma}}}) = -0.135$ for the entire integration, the motion became oscillatory about the heat-shield-forward trim point after one cycle of the initial large amplitude motion (i.e., at $t \sim 0.101$ sec). However, with $(C_{m_q} + C_{m_{\dot{\sigma}}}) = -0.135$ for this mode the frequency and amplitude of the synthesized motion did not show an acceptable match to the frequency and amplitude of the observed motion beyond $t \sim 0.101$ second. Therefore, different values of $(C_{m_q} + C_{m_{\dot{\sigma}}})$ were tried and the value $(C_{m_q} + C_{m_{\dot{\sigma}}}) = -0.02$ was found to produce the best match for $t > 0.101$ second. (The motion history shows divergence despite a stable damping parameter because of the decreasing dynamic pressure.) This value was arbitrarily injected at the first peak of the heat-shield-forward mode (i.e., $t = 0.101$ sec). As can be seen, the model oscillates about a trim angle of $\sim 155^\circ$ in this mode. In general, the synthesized motion matches the observed data points extremely well. However, as time increased, the observed motion became less planar and the last cycle of the heat-shield-forward motion exhibited a somewhat elliptical motion. Hence, the agreement between observed and synthetic results is not as good for the latter portion of the motion.

For the second flight (fig. 8(b)) the model was launched at an initial Mach number of 0.98 and decelerated to $M = 0.71$. The initial conditions for the synthesized motion were $\sigma_i = 210^\circ$, $\dot{\sigma}_i = 0$, at $t_i = 0.042$ second. A value of $(C_{m_q} + C_{m_{\dot{\sigma}}}) = -0.07$ was used to obtain the synthetic curve, which is reasonably close to the value of -0.135 found to apply in the earlier portion of the first flight. It is immediately apparent that the motion for this case is somewhat different from that in figure 8(a). The data in figure 8(b) show two large angular excursions as contrasted to one for the previous case. An attempt was made to determine the principal cause for this difference. Synthetic motions for each test were computed from all possible (i.e., four) combinations of $\alpha_i = 200^\circ$, 210°, and the two selected damping values $(C_{m_q} + C_{m_{\dot{\sigma}}}) = -0.07$, -0.135. A comparison of the eight synthesized motions (four from each of the two tests) led to the conclusion that no single cause would account for the difference in the observed motions. The influencing factors are several: (1) the Mach number difference, (2) the difference in initial amplitude, which is affected by both Mach number and sabot separation, and (3) the damping value used, which is influenced by Mach number and the angle-of-attack range. Regardless of the cause, though, these differences in motion characteristics are well predicted by synthetic curves.

Both of the synthesized motions produced for the strake configurations showed that the over-all shape of the curve (as defined by both frequency and

amplitude histories) was very sensitive to a small change in $(C_{m_q} + C_{m_{\dot{\alpha}}})$. (This is also true to a lesser extent for the other two configurations.) For bodies with small damping moments and linear static moments that are not functions of Mach number, a change in the damping parameter would affect only the amplitude of the motion and the frequency would be relatively unchanged. However, with nonlinear moments and/or moments dependent on Mach number, as we have here, a change in damping affects not only the amplitude but the frequency as well. In some cases a change in the damping coefficient forces the motion into oscillations about another stable trim point at some instant in the motion history. Because the shape of the curve is quite sensitive to the damping values used, it is felt that the effective value of $(C_{m_q} + C_{m_{\dot{\alpha}}})$ which produces the motion best matching a given set of observed points is determined fairly accurately and is representative of an average damping coefficient for the angle-of-attack range considered.

Command Module Plus Tower With Flap

The command module plus tower with flap was tested at three different Mach numbers and the motion histories are shown in figure 9.

In figure 9(a) the initial Mach number was 1.00 and the model decelerated to $M = 0.81$. (The model was in view through 13 stations only.) Three curves are shown, one being a faired plot through the observed data points and two being synthetic curves generated from the computer program. The initial conditions for the synthesized motions were $\sigma_i = 285^\circ$, $\dot{\sigma}_i = 0$, at $t_i = 0.042$ second. From a comparison of the synthesized motions with the observed motion it is immediately apparent that the two motions are similar (i.e., show oscillations between $\sim 285^\circ$ and $\sim 0^\circ$) but differ considerably in frequency. The frequency of the observed motion is higher than that predicted by the synthesized motion. The observed motion also appears to have a slightly higher trim angle than the synthesized motion. The difference in frequency might be expected because the tower members of the free-flight model were oversized by about 75 percent in diameter for additional strength. Therefore, at any σ other than the trim angle of attack, the resulting absolute value of the pitching moment would be higher (tower structure is forward of center of gravity) for the oversized tower members than for a perfectly scaled version such as used in the wind-tunnel tests. This increased moment would then produce an increase in frequency.

As was mentioned in the discussion on data reduction, wind-tunnel dynamic data $(C_{m_q} + C_{m_{\dot{\alpha}}})$ versus α were available for this configuration, and a motion was synthesized both with these data and with a constant value of $(C_{m_q} + C_{m_{\dot{\alpha}}})$. The data used for $(C_{m_q} + C_{m_{\dot{\alpha}}})$ versus α were for $M = 0.8$, which were the only data available near the Mach number range of this test. A constant value of $(C_{m_q} + C_{m_{\dot{\alpha}}}) = -0.15$ was used for the constant damping. It is apparent that the motion with constant damping and with variable damping are nearly identical. This illustrates that, for this case at least, there is an effective constant value of damping which represents the variable damping coefficient quite well.

8

In figure 9(b) the initial Mach number was 0.62 and the model decelerated to M = 0.48. (The model swerved out of view after 21 stations). Again three curves are shown: a faired curve through the observed points and two synthetic curves. As in figure 9(a) two synthesized motions were produced, one for variable damping, and one for constant damping. For the variable damping case, $(C_{m_q} + C_{m_{\dot\alpha}})$ versus α for M = 0.5 was used. A constant value of $(C_{m_q} + C_{m_{\dot\alpha}})$ = 0.10 was found best for the constant damping case. The initial conditions for the synthesized motions were σ_i = 310°, $\dot\sigma_i$ = 0, at t_i = 0.068 second. Immediately apparent in figure 9(b), in contrast to the motion in figure 9(a) at a higher Mach number, is the fact that the model tumbles after returning from a maximum amplitude of ~310°. It appears then that a decrease in the over-all Mach number range or a higher initial amplitude causes the model to go into a tumbling mode. An effort was made to determine the primary cause for this difference in motion. By computing synthesized motions for each test for all possible combinations of α_i = 310°, 285°, and $(C_{m_q} + C_{m_{\dot\alpha}})$ = +0.10, -0.15, it was found that the principal factor which produced different motion characteristics was the value of damping that was used. The damping characteristics depend on Mach number and angle-of-attack range. Therefore, the difference in motion is affected by <u>both</u> a Mach number difference and a difference in initial amplitude.

Also apparent in figure 9(b) is the difference in frequency for the observed and synthetic curves caused by the oversized tower members in the free-flight model. Another noticeable difference is that the tumbling rate observed in the actual motion appears to decrease with time, whereas the synthesized motions show tumbling rates that increase with time. This difference may be due to the fact that the syntheses using constant damping or variable damping at only one Mach number are not really quite representative of what is actually being felt by the model in flight. The value of $(C_{m_q} + C_{m_{\dot\alpha}})$ = 0.10 was chosen as best for constant damping because it agreed best with the observed tumbling rate over the entire length of time. However, a value of $(C_{m_q} + C_{m_{\dot\alpha}})$ = 0.20 produced a curve whose tumbling rate agreed more closely with that of the variable damping case.

Figure 9(c) shows a faired plot through the observed data points for a test with initial and final Mach numbers of 0.40 and 0.33, respectively. No wind-tunnel data were available for this Mach number range so no synthesis was attempted. However, it can be seen that the resulting motion exhibits nearly identical characteristics to the observed motion in figure 9(b) at M = 0.62 to M = 0.48. Therefore, it appears that the over-all behavior of the model is not a strong function of Mach number in the lower subsonic range.

CONCLUSIONS

The Apollo command module alone and two proposed abort configurations were tested in free flight in the apex-forward attitude and the resulting motions were compared to motions computed from conventional wind-tunnel data. The following conclusions were made:

1. Angular motion histories, synthesized by the use of conventional wind-tunnel aerodynamic data, showed good agreement with the large amplitude, nearly planar motions observed in free flight. Effective values for aerodynamic damping can be obtained by this technique.

2. The command module alone is statically and dynamically stable at a trim angle of attack of $36°$ up to at least $M = 2.0$.

3. The command module with strakes rotates so that its heat shield is forward ($180°$) but does not immediately stabilize in this position. Depending on Mach number and initial rotation rate, the model oscillates between $0°$ and $\sim200°$ for one or more cycles.

4. The command module plus tower with flap rotates initially from apex foward ($0°$) to an amplitude of $\sim300°$ and returns to $\sim0°$. For low subsonic speeds it passes on through $0°$ and tumbles. For high subsonic speeds it appears to oscillate between $\sim0°$ and $\sim300°$ and does not tumble.

Ames Research Center
 National Aeronautics and Space Administration
  Moffett Field, Calif., May 14, 1965

APPENDIX A

EQUATIONS OF PITCHING MOTION FOR A BODY IN DECELERATING

FREE FLIGHT AT CONSTANT AMBIENT PRESSURE
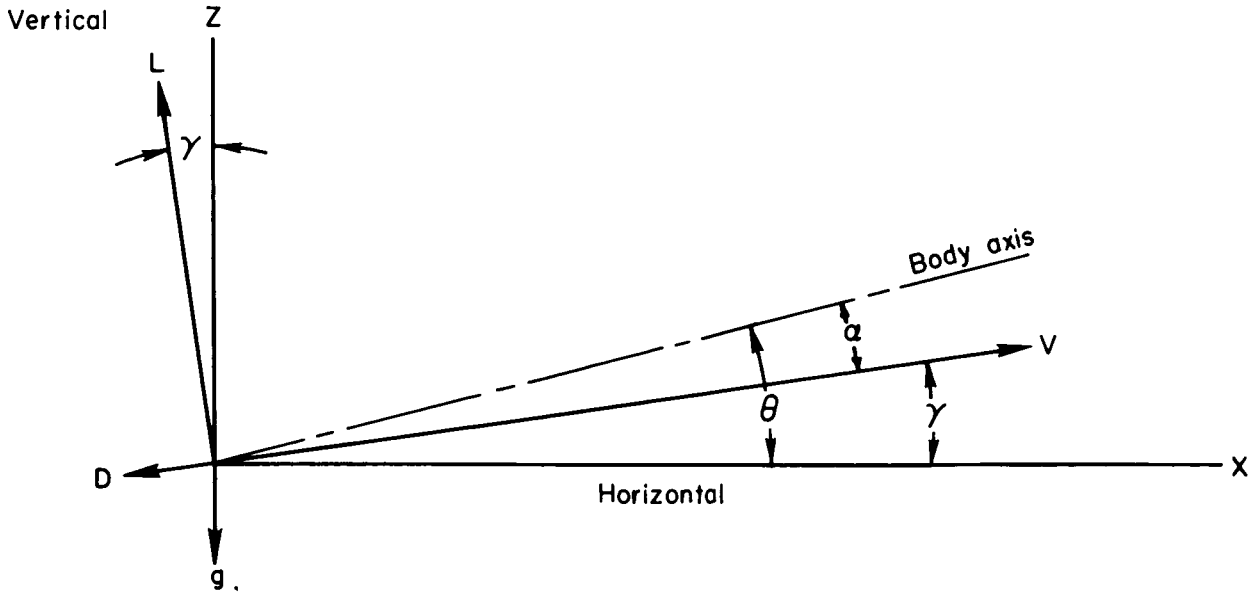
The differential equations of planar motion of a body oscillating in pitch are

$$I_y \ddot{\theta} = C_m q A d + C_{m_q}\left(\frac{d}{V}\right) q A d \dot{\theta} + C_{m_{\dot{\alpha}}}\left(\frac{d}{V}\right) q A d \dot{\alpha} \tag{A1}$$

where

$$C_{m_q} = \frac{\partial C_m}{\partial\left(\frac{\dot{\theta} d}{V}\right)} \; , \qquad C_{m_{\dot{\alpha}}} = \frac{\partial C_m}{\partial\left(\frac{\dot{\alpha} d}{V}\right)}$$

$$\ddot{Z} = \frac{L}{M} - g = \frac{C_L q A}{m} - g \tag{A2}$$

where g is gravitational acceleration and

$$\ddot{X} = \ddot{V} \cos \gamma - V\dot{\gamma} \sin \gamma \cong \dot{V} \; (\text{for small } \gamma) \tag{A3}$$

Note that $\dot{V} = -(D/m) - g \sin \gamma \, (g \sin \gamma \sim 0)$; therefore, D is accounted for in the $\dot{V}$ term.

In the above equations

$$V = V(t)$$

$$q = q(t)$$

$$C_m = C_{m_1}(M,\alpha) = C_{m_2}(V,\alpha) = C_m(t)$$

$$C_L = C_{L_1}(M,\alpha) = C_{L_2}(V,\alpha) = C_L(t)$$

$$C_{m_q} + C_{m_{\dot{\alpha}}} = f_1(M,\alpha) = f_2(V,\alpha) = f(t)$$

or in some cases

$$C_{m_q} + C_{m_{\dot{\alpha}}} = \text{constant}$$

From the above sketch

$$\theta = \gamma + \alpha \tag{A4a}$$

$$\dot{\theta} = \dot{\gamma} + \dot{\alpha} \tag{A4b}$$

$$\ddot{\theta} = \ddot{\gamma} + \ddot{\alpha} \tag{A4c}$$

also

$$\left.\begin{array}{l} \dot{Z} = V \sin \gamma \cong V\gamma \\[2mm] \ddot{Z} = V\dot{\gamma} + \dot{V}\gamma \end{array}\right\} \quad (\text{for small } \gamma) \tag{A5}$$

Solving for $\dot{\gamma}$ in equation (A5) and substituting for $\ddot{Z}$ from (A2) one gets

$$\dot{\gamma} = \frac{1}{V}\left(\frac{C_L q A}{m} - g - \gamma\dot{V}\right) \tag{A6a}$$

If $\rho V^2/2$ is substituted for q

$$\dot{\gamma} = \frac{\rho A V}{2m} C_L - \frac{\gamma}{V}\dot{V} - \frac{g}{V} \tag{A6b}$$

$$\ddot{\gamma} = \frac{\rho A V}{2m}\frac{dC_L}{dt} + \frac{\rho A C_L}{2m}\dot{V} - \frac{\dot{V}}{V}\dot{\gamma} - \frac{\gamma}{V}\frac{d\dot{V}}{dt} + \frac{\gamma\dot{V}^2}{V^2} + \frac{g\dot{V}}{V^2} \tag{A6c}$$

Note

$$\frac{dC_L}{dt} = \frac{\partial C_L}{\partial \alpha}\frac{d\alpha}{dt} + \frac{\partial C_L}{\partial V}\frac{dV}{dt} = C_{L_\alpha}\dot{\alpha} + \frac{\partial C_L}{\partial V}\dot{V} \tag{A6d}$$

where C_{L_α} is the local slope along the curve of C_L versus α. By substituting equation (A6b) into equation (A4b) for $\dot{\gamma}$ and equation (A6c) into equation (A4c) for $\ddot{\gamma}$ and then in turn substituting equation (A4b) and equation (A4c) into equation (A1) for $\dot{\theta}$ and $\ddot{\theta}$, one obtains

$$I_y\left[\frac{\rho AV}{2m}\left(C_{L_\alpha}\dot{\alpha} + \frac{\partial C_L}{\partial V}\dot{V}\right) + 2\gamma\left(\frac{\dot{V}}{V}\right)^2 - \frac{\gamma}{V}\frac{d\dot{V}}{dt} + 2g\frac{\dot{V}}{V^2} + \ddot{\alpha}\right]$$

$$= C_m\frac{\rho AdV^2}{2} + C_{m_q}\left(\frac{d}{V}\right)\frac{\rho V^2}{2}Ad\left(\frac{\rho AV}{2m}C_L - \frac{\gamma\dot{V}}{V} - \frac{g}{V} + \dot{\alpha}\right) + C_{m_{\dot{\alpha}}}\left(\frac{d}{V}\right)\frac{\rho V^2}{2}Ad\dot{\alpha}$$

$$\tag{A7a}$$

Simplifying and using the relation

$$I_y = mr_g^2 \tag{A7b}$$

we have

$$\ddot{\alpha} - \frac{\rho AV}{2m}\left[\left(C_{m_q} + C_{m_{\dot{\alpha}}}\right)\left(\frac{d}{r_g}\right)^2 - C_{L_\alpha}\right]\dot{\alpha} - C_m\frac{\rho AV^2d}{2I_y} - C_{m_q}C_L\left(\frac{\rho AV}{2m}\right)^2\left(\frac{d}{r_g}\right)^2$$

$$+ C_{m_q}\frac{\rho A}{2m}\left(\frac{d}{r_g}\right)^2 g + 2g\frac{\dot{V}}{V^2} + \left[C_{m_q}\frac{\rho A}{2m}\left(\frac{d}{r_g}\right)^2\dot{V} + 2\left(\frac{\dot{V}}{V}\right)^2 - \frac{1}{V}\frac{d\dot{V}}{dt}\right]\gamma + \frac{\rho AV}{2m}\frac{\partial C_L}{\partial V}\dot{V} = 0$$

$$\tag{A8}$$

For the conditions of these tests, all the terms following the first three are negligible compared to the third term, $C_m(\rho AV^2d/2I_y)$, and the final equation of motion is

$$\ddot{\alpha} - \frac{\rho AV}{2m}\left[\left(C_{m_q} + C_{m_{\dot{\alpha}}}\right)\left(\frac{d}{r_g}\right)^2 - C_{L_\alpha}\right]\dot{\alpha} - C_m\frac{\rho AV^2d}{2I_y} = 0 \tag{A9}$$

To generalize the above equation for any planar motion case and not just a motion in the vertical plane, substitute σ (the resultant planar angle of attack) for α in equation (A9).

$$\ddot{\sigma} - \frac{\rho AV}{2m}\left[\left(C_{m_q} + C_{m_{\dot{\sigma}}}\right)\left(\frac{d}{r_g}\right)^2 - C_{L_\sigma}\right]\dot{\sigma} - C_m\frac{\rho AV^2d}{2I_y} = 0 \tag{A10}$$

TABLE I.- MODEL CHARACTERISTICS AND TEST CONDITIONS

Physical characteristics of models						
Run	d, cm	$\dfrac{X_{cg}}{d}$	$\dfrac{Z_{cg}}{d}$	$\left(\dfrac{d}{r_g}\right)^2$	m, kg	$I_y \times 10^5$, kg-m^2
628[a]	5.085	0.291	0.053	20.05	0.17126	2.21
629[a]	5.085	.291	.053	20.05	.17126	2.21
630[a]	5.085	.291	.053	20.09	.17192	2.21
632[a]	5.085	.291	.053	20.05	.17126	2.21
641[b]	5.082	.293	.054	19.99	.17157	2.22
642[b]	5.082	.293	.054	19.99	.17157	2.22
656[c]	5.082	.352	.049	11.78	.18665	4.09
659[c]	5.082	.346	.050	11.71	.18679	4.12
661[c]	5.082	.342	.049	12.21	.18579	4.43

[a] command module
[b] command module with strakes
[c] command module with tower and flap

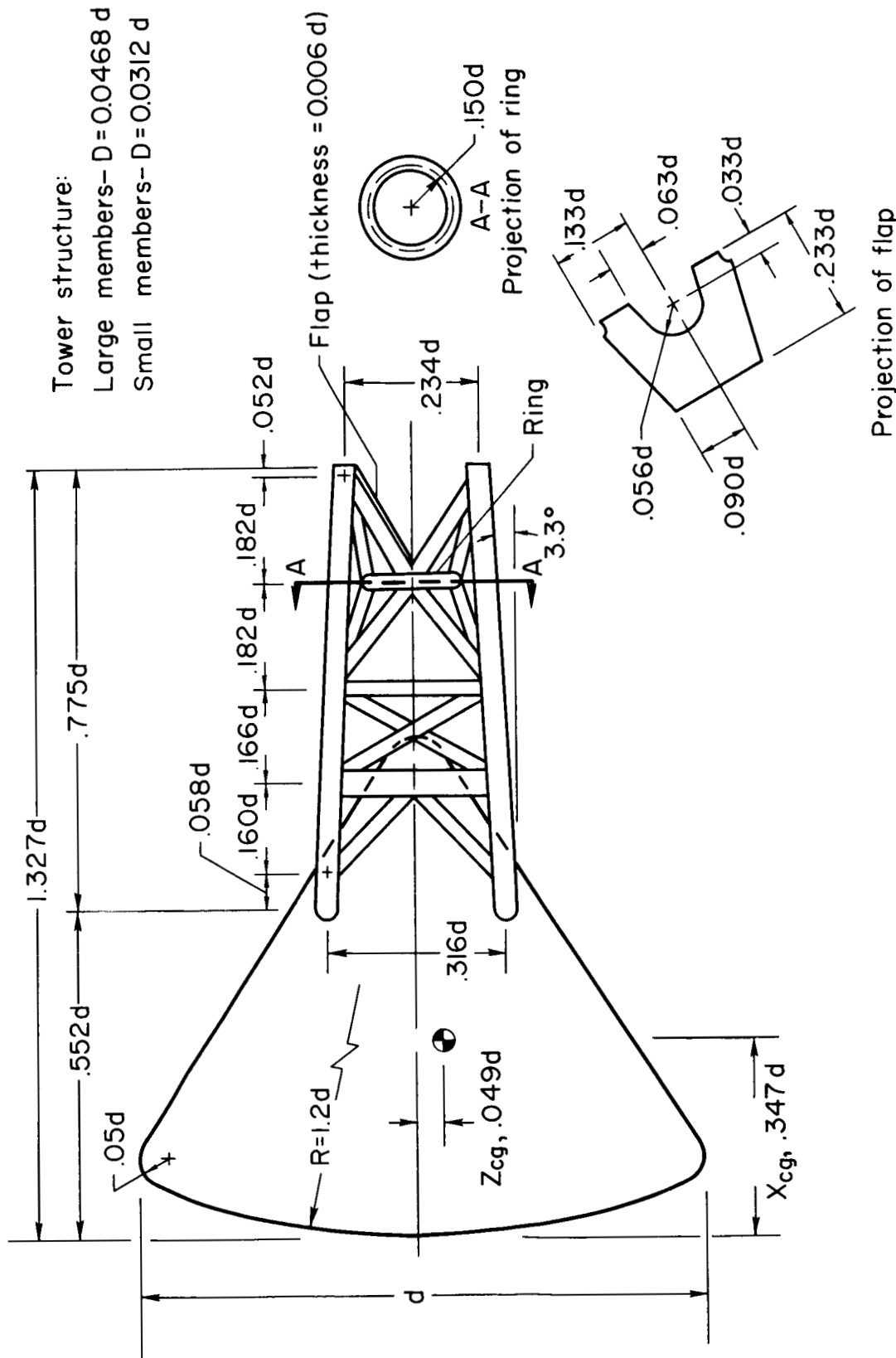| Test conditions						
Run	M_i	M_f	V_i, m/sec	V_f, m/sec	$R_i \times 10^{-6}$	$R_f \times 10^{-6}$	ρ, kg/m^3
628	0.71	0.67	245.7	229.8	0.82	0.76	1.195
629	1.18	1.06	408.4	365.8	1.19	1.07	1.192
630	1.13	.98	397.8	346.2	3.67	3.19	3.298
632	2.05	1.29	707.1	445.0	2.36	1.48	1.201
641	1.10	.73	378.1	249.9	1.28	.85	1.213
642	.98	.71	338.3	246.0	1.09	.80	1.174
656	.62	.47	211.2	161.2	.75	.57	1.244
659	.40	.33	135.0	110.3	.48	.40	1.253
661	1.10	.81	341.4	278.3	1.18	.97	1.234

Front view

Top view

Strakes

.04 d

.0595d

.216d

R=1.2 d

33° 26'

.32 d

.735d

.877d

X$_{cg}$,
.293 d

.05 d

.03 d

d

Z$_{cg}$,
.054 d

.01 d
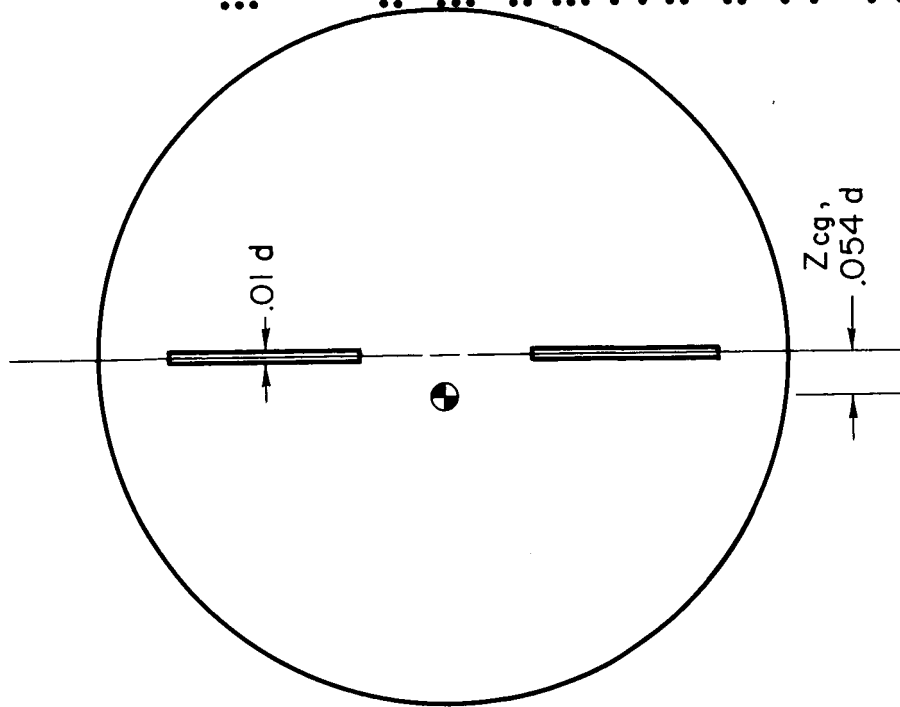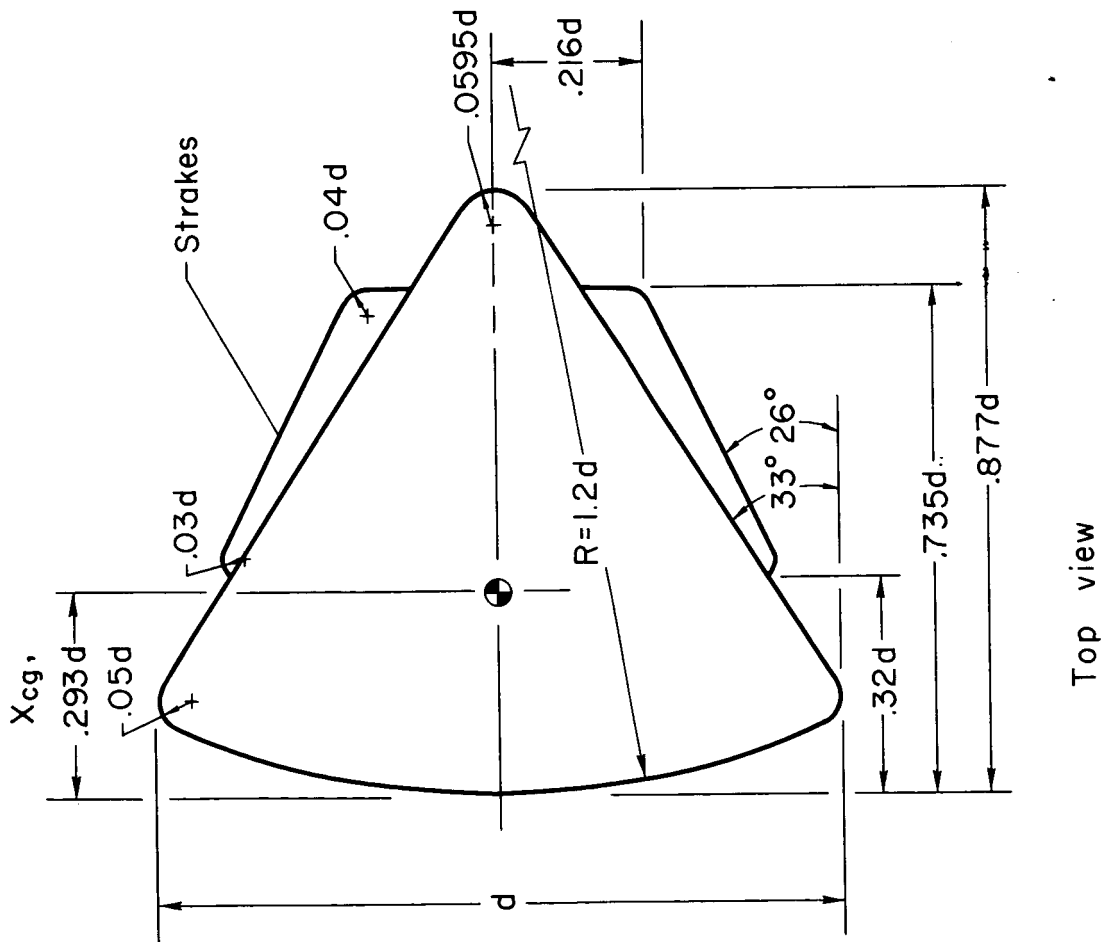
(a) Command module with strakes.

Figure 1.- Sketch of turn-around models.

Tower structure:
Large members– D = 0.0468 d
Small members– D = 0.0312 d

Flap (thickness = 0.006 d)

.150d

A–A
Projection of ring

.133d

.063d

.033d

.056d

.233d

.090d

Projection of flap

.052d

.182d

.234d

Ring

3.3°

.182d

.058d

.166d .182d

.160d

1.327d

.775d

.316d

.552d

.05d

R = 1.2d

Z_cg, .049d

X_cg, .347 d

d

Side view

(b) Command module plus tower with flap.

Figure 1.– Concluded.
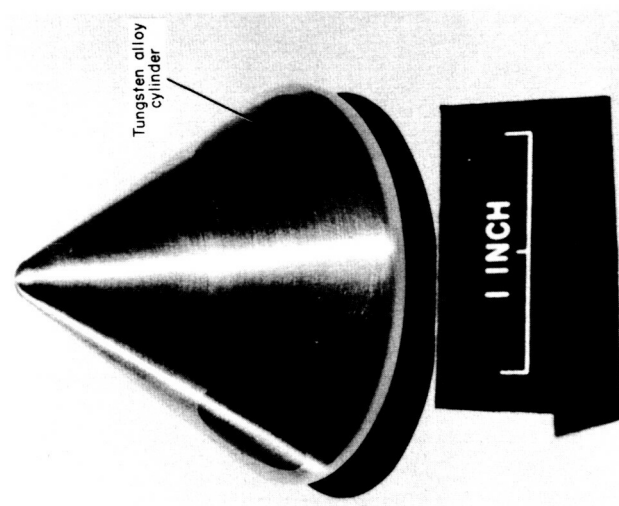
A-31673

(c) Command module plus tower with flap.

A-31674

(b) Command module with strakes.

Figure 2.- Photographs of models.

A-31675.1

Tungsten alloy cylinder

(a) Command module alone.
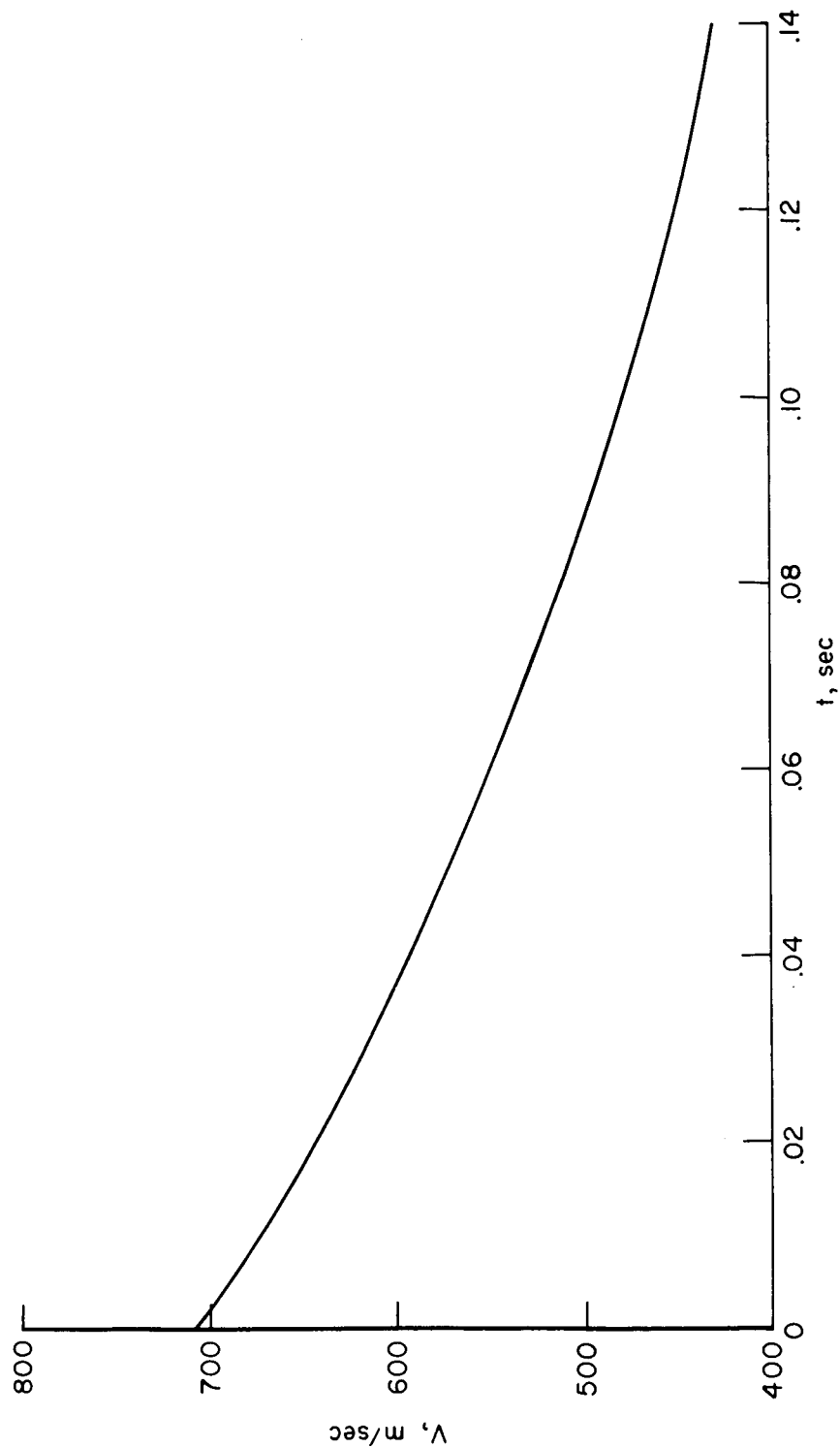
Figure 3.- Typical velocity variation.
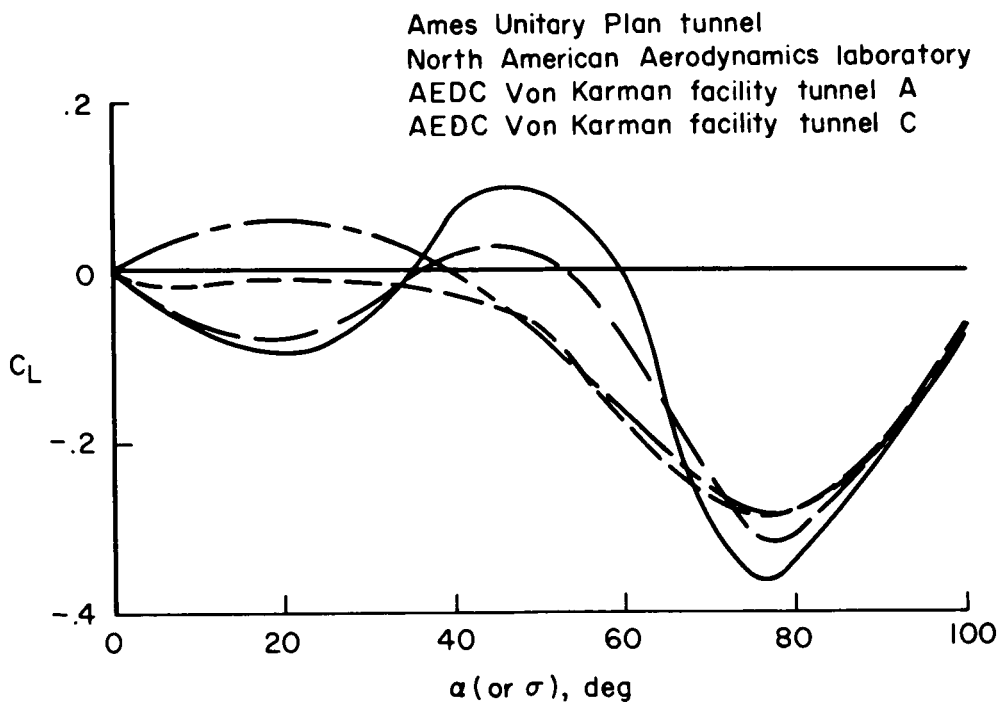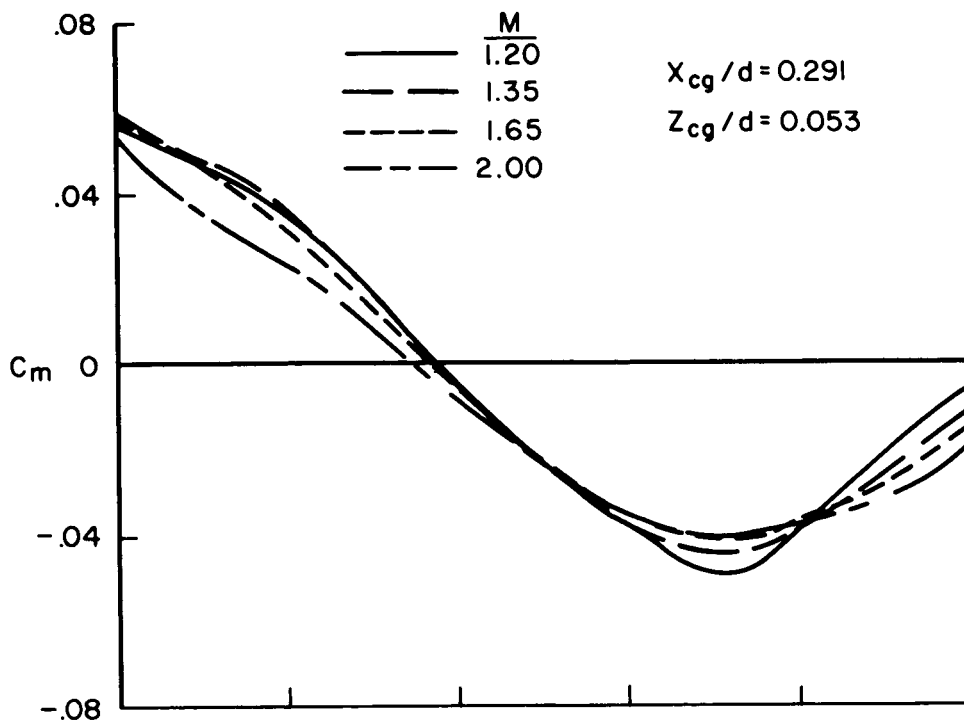
(a) Command module alone.

Figure 4.- Pitching-moment and lift-coefficient data from wind-tunnel tests.
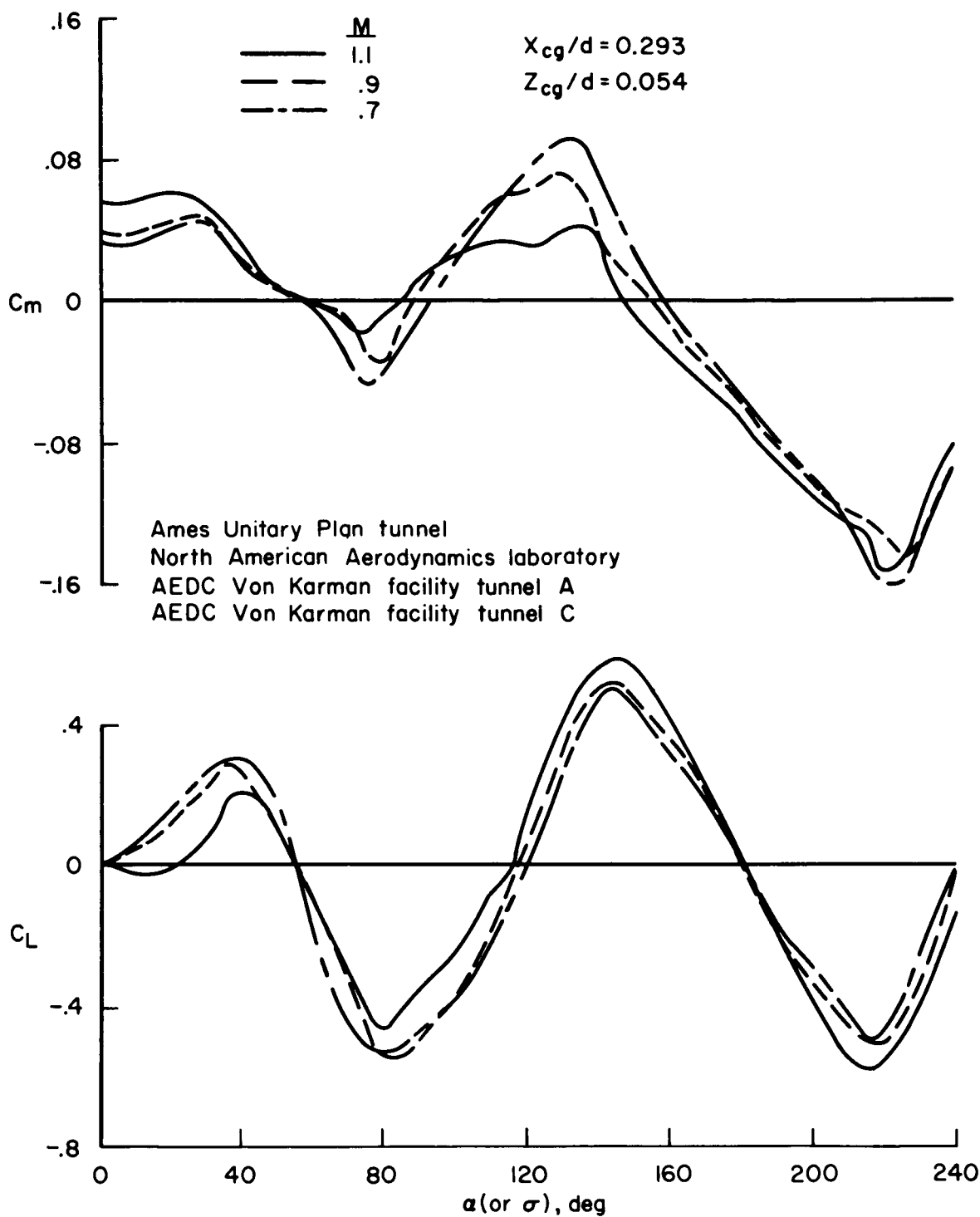
(b) Command module with strakes.

Figure 4.- Continued.
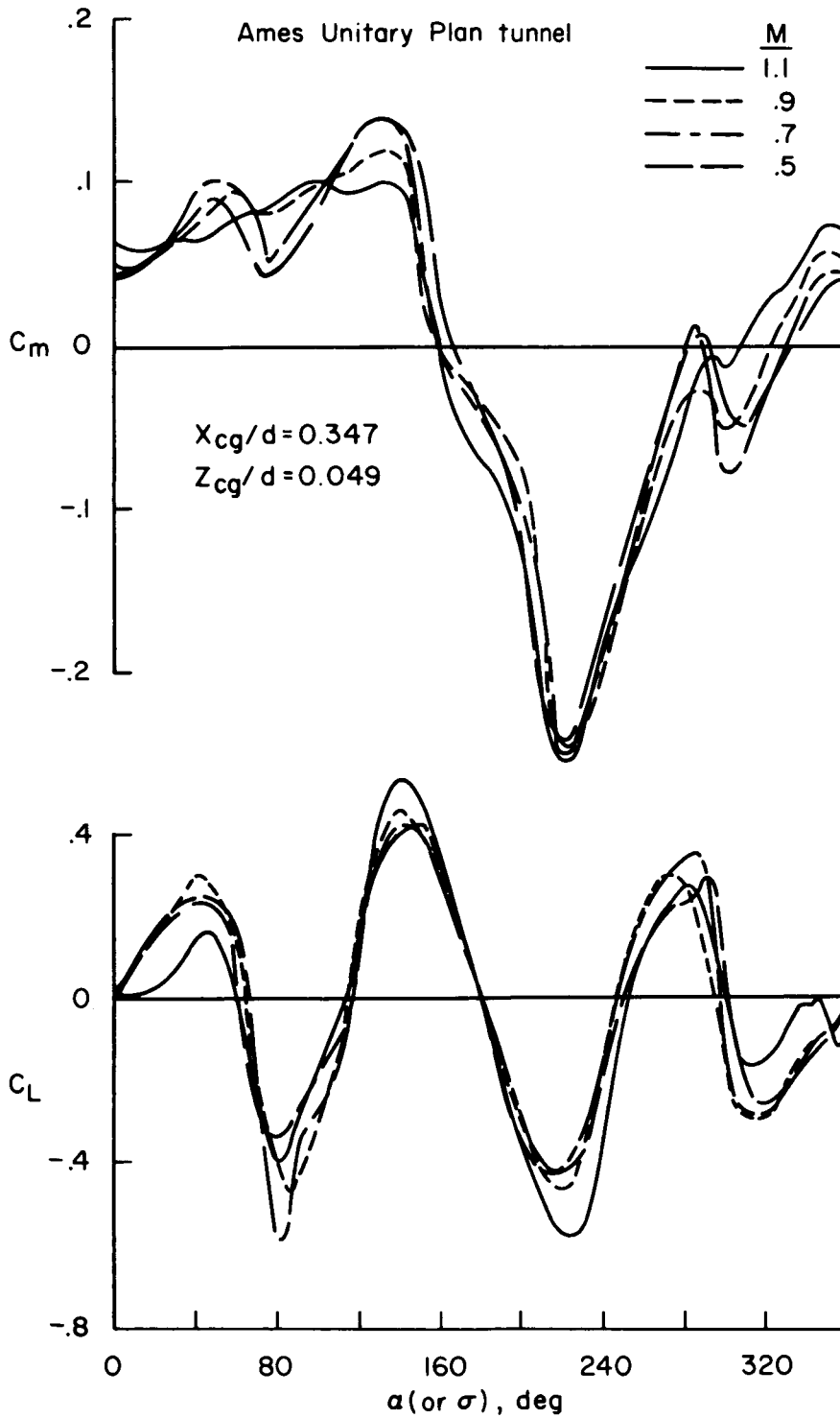
(c) Command module plus tower with flap.

Figure 4.- Concluded.
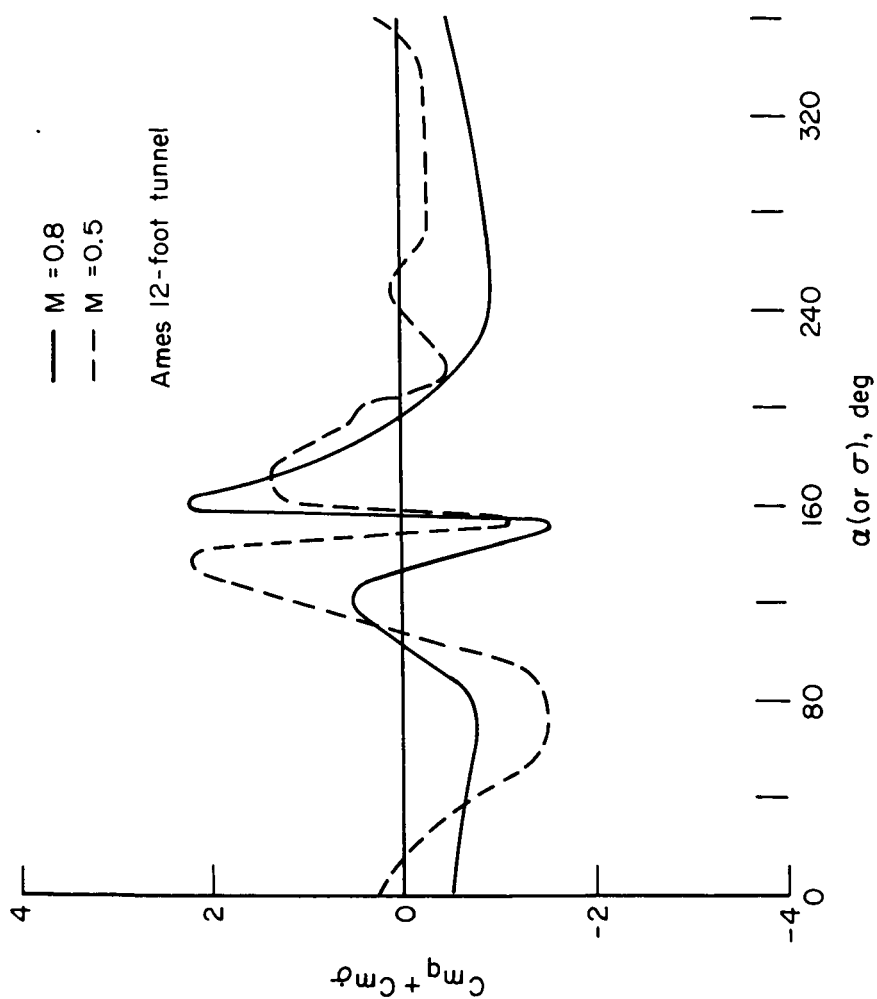
Figure 5.- Damping-in-pitch coefficient versus angle of attack for command module plus tower with flap from wind-tunnel tests.
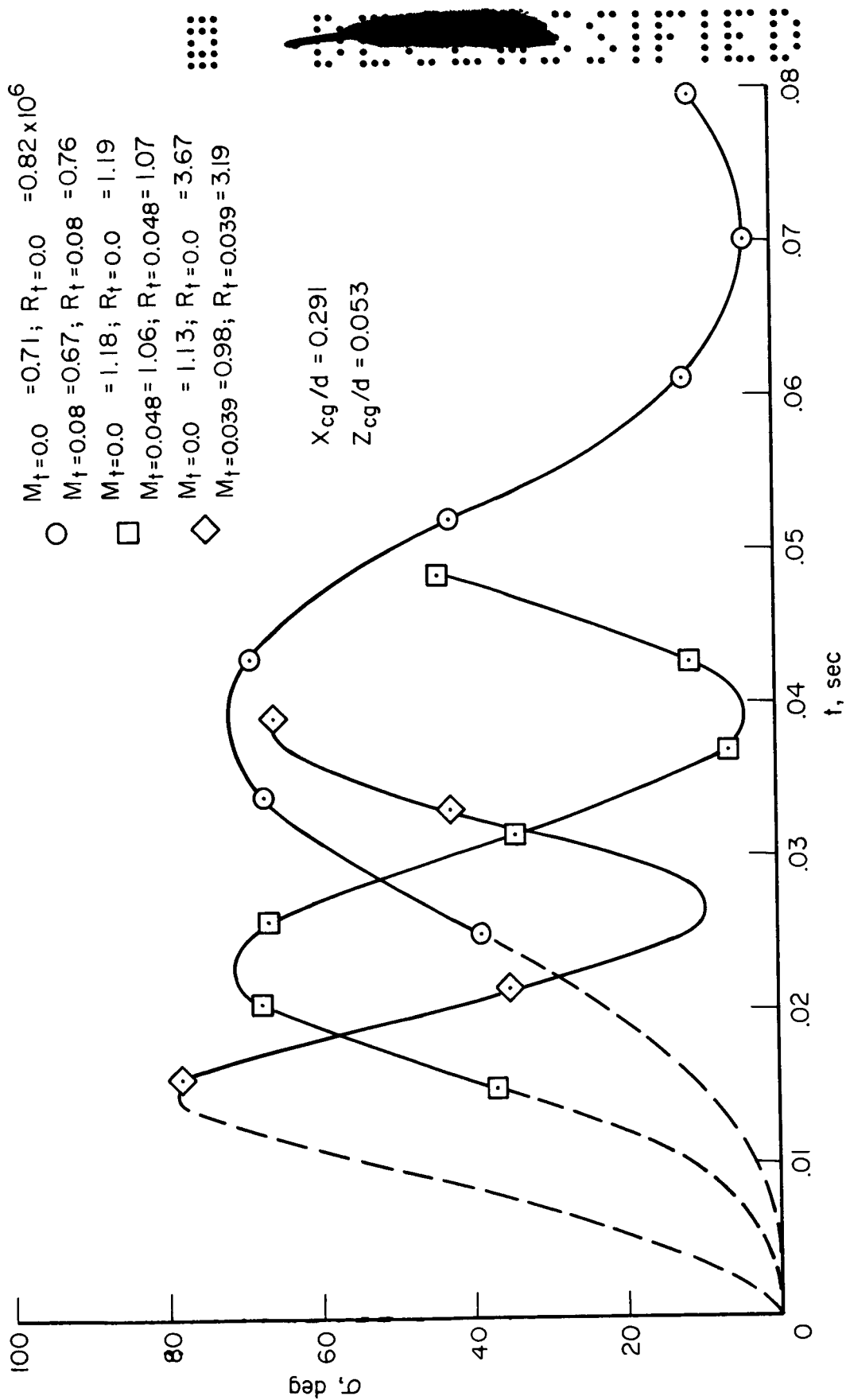
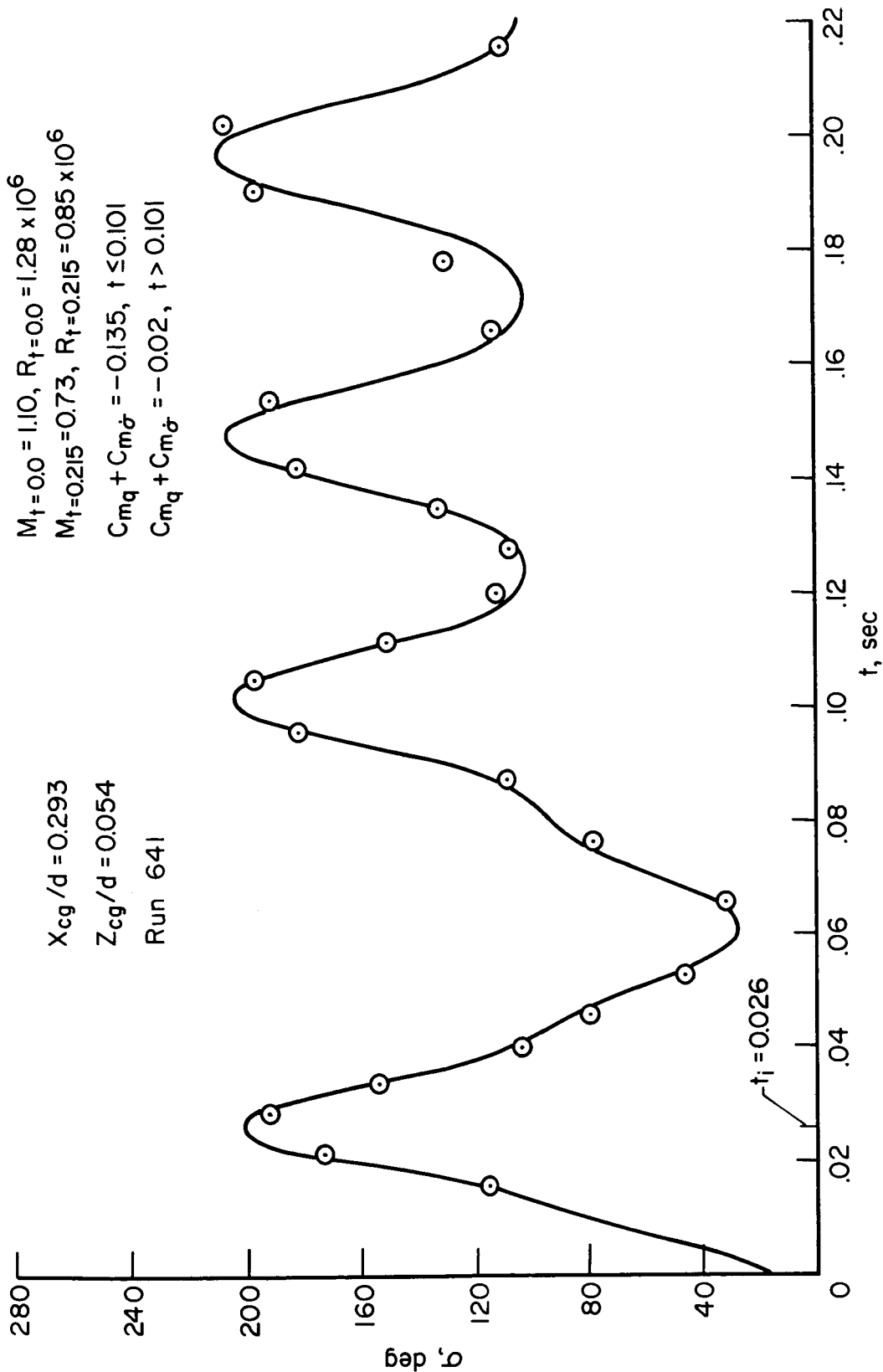Figure 6.- Observed motions of command module alone for short-distance flights.
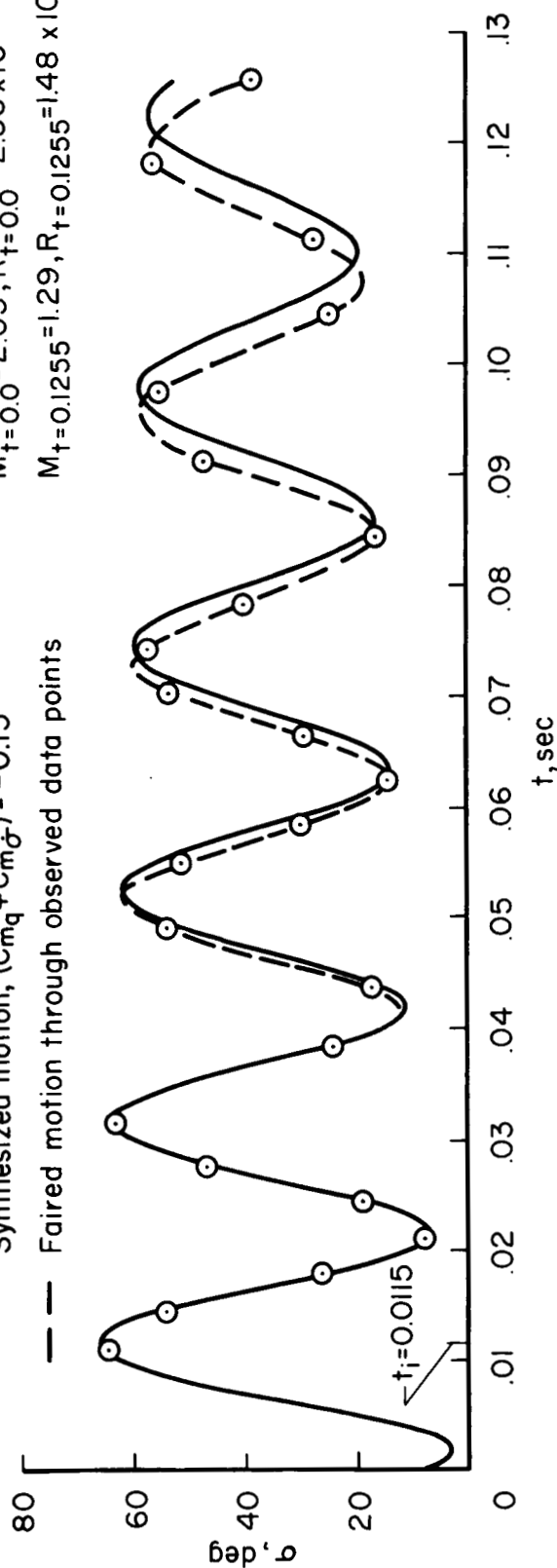
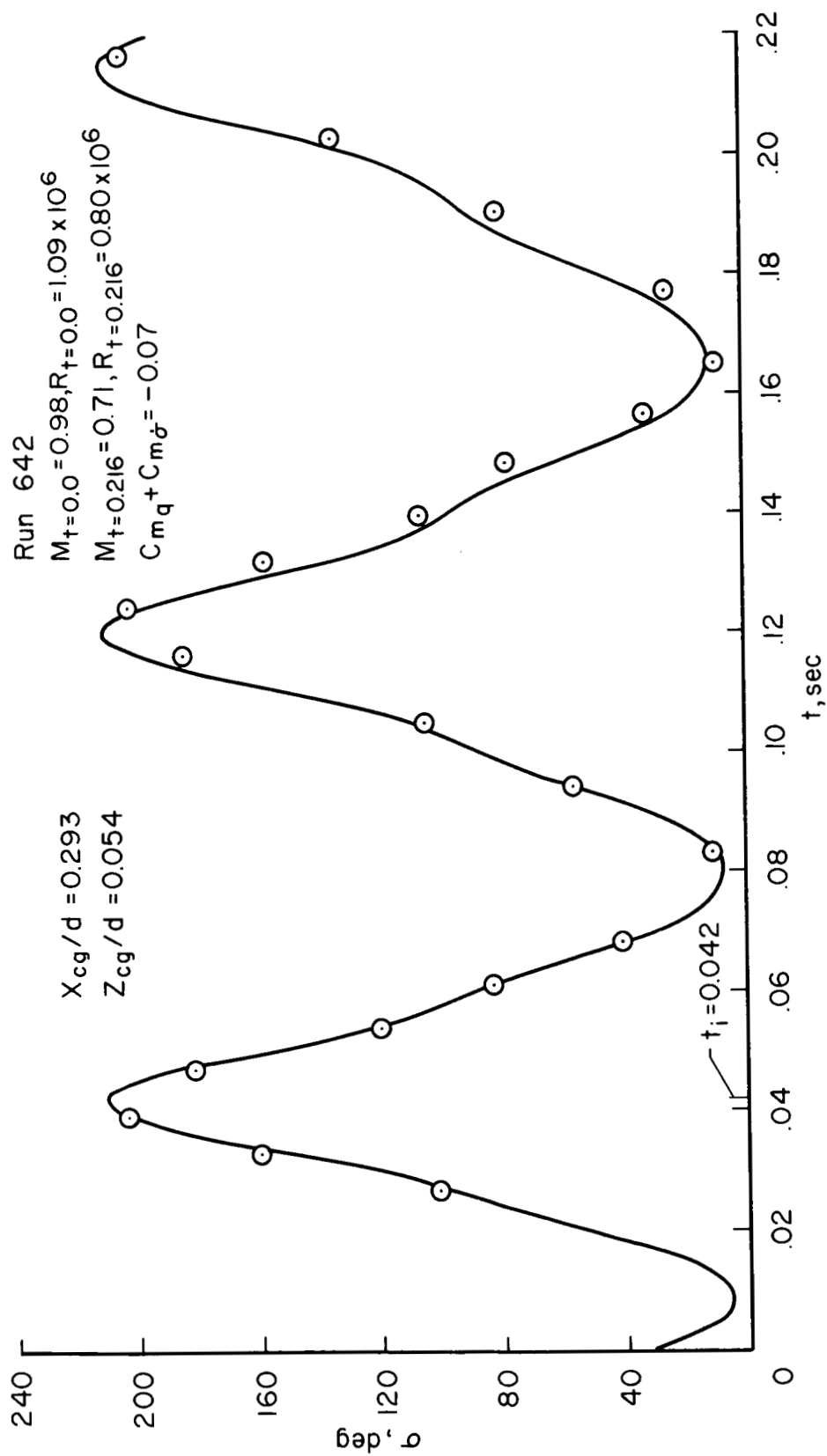Figure 7.- Observed and synthesized motions for command module alone.

(a) Initial $M = 1.10$.

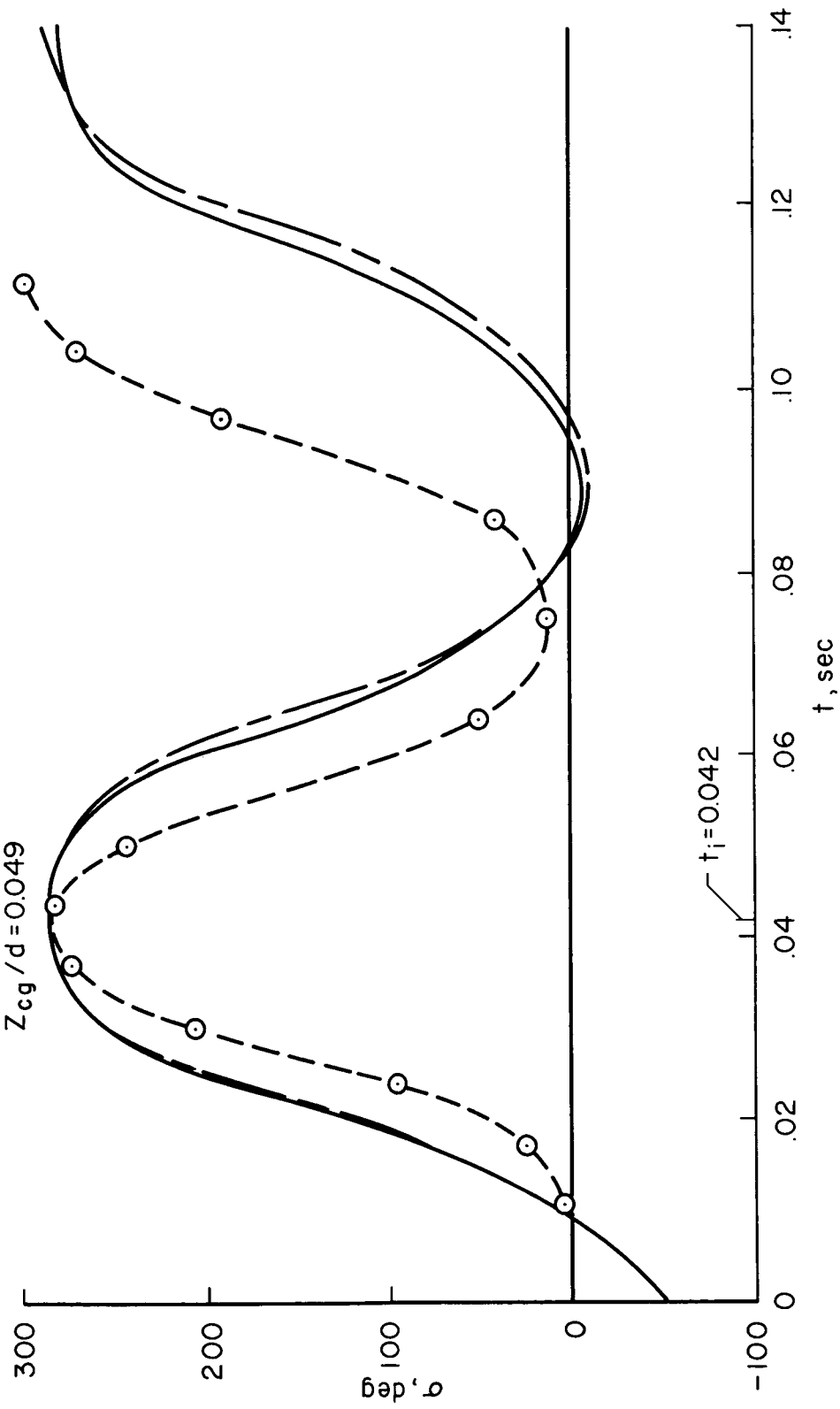Figure 8.– Synthesized motion and observed data points for command module with strakes.

Run 642
$M_{t=0.0} = 0.98, R_{t=0.0} = 1.09 \times 10^6$
$M_{t=0.216} = 0.71, R_{t=0.216} = 0.80 \times 10^6$
$C_{m_q} + C_{m_{\dot{\alpha}}} = -0.07$

$X_{cg}/d = 0.293$
$Z_{cg}/d = 0.054$

$t_i = 0.042$

σ, deg

t, sec

(b) Initial $M = 0.98$.

Figure 8.- Concluded.

(a) Observed and synthesized motions at initial $M = 1.00$.

Figure 9.- Motions of command module plus tower with flap.

Run 656
$M_{t=0.0}=0.62, R_{t=0.0}=0.75 \times 10^6$
$M_{t=0.307}=0.48, R_{t=0.307}=0.58 \times 10^6$

——— $(C_{m_q}+C_{m_{\dot\sigma}})=0.10$
——— Faired plot through data
——— $(C_{m_q}+C_{m_{\dot\sigma}})=f(\sigma)$ @ M=0.5
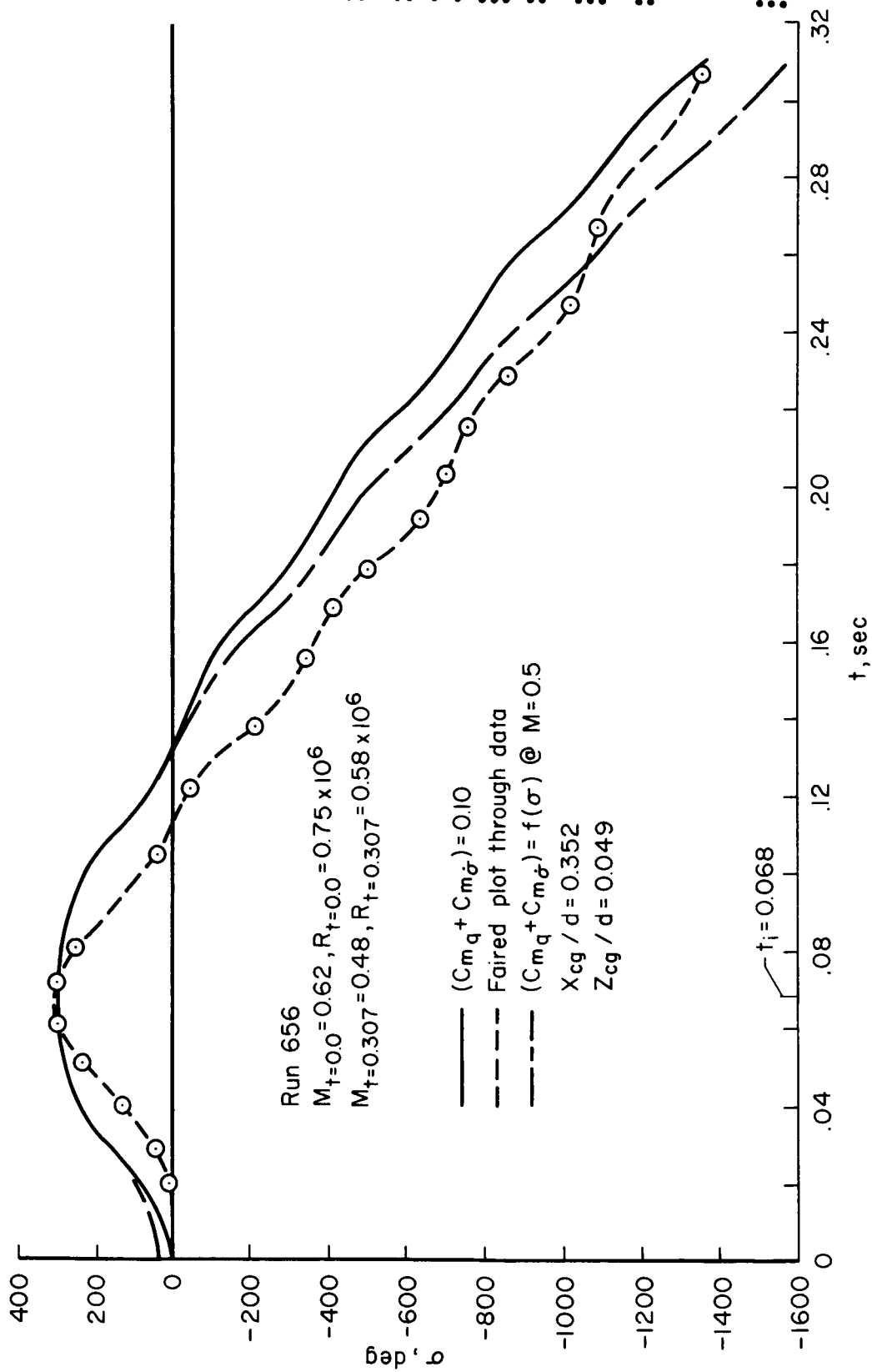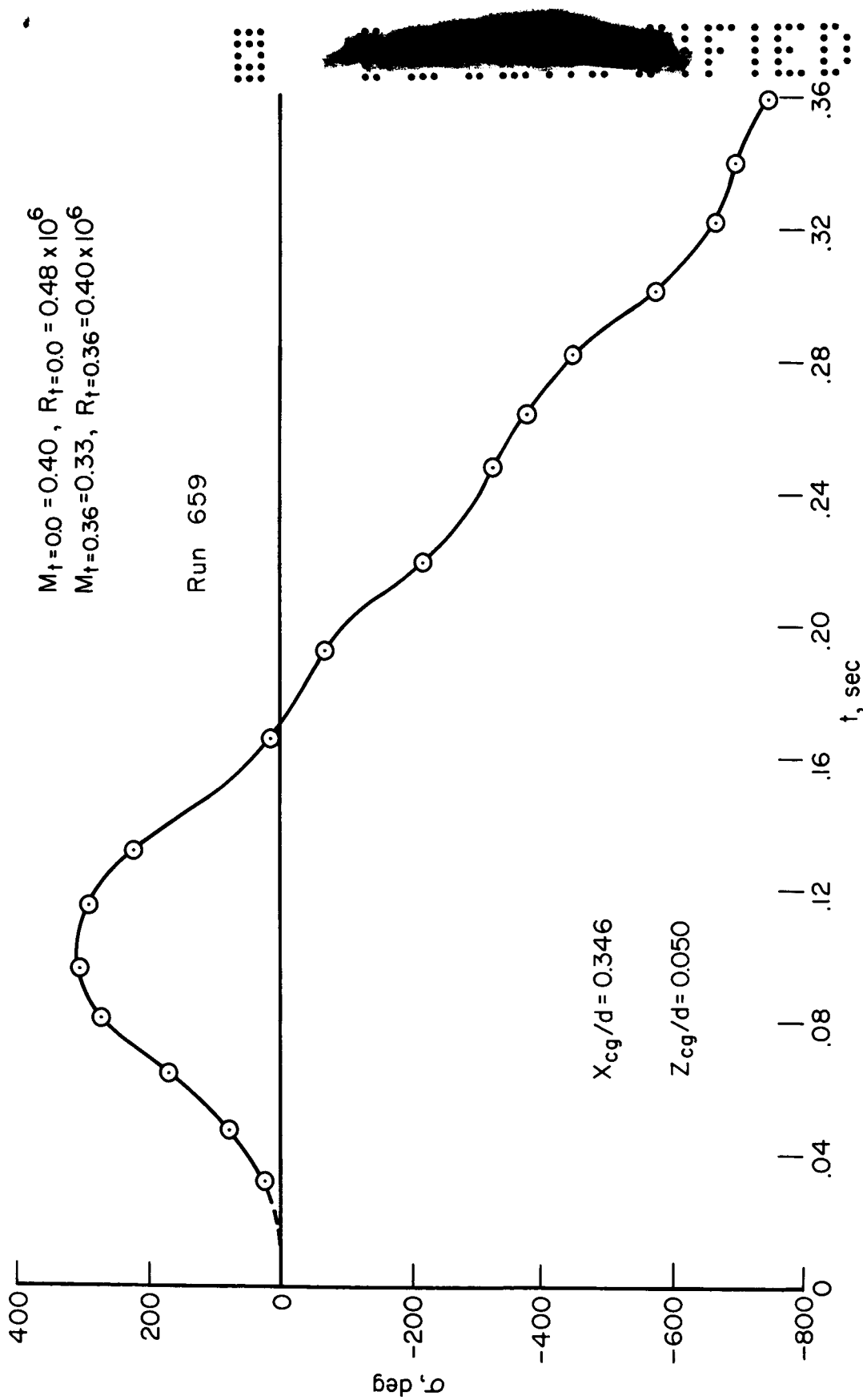$X_{cg}/d=0.352$
$Z_{cg}/d=0.049$

$t_i=0.068$

(b) Observed and synthesized motions at initial $M=0.62$.

Figure 9.- Continued.

(c) Observed motion at initial M = 0.40.

Figure 9.- Concluded.